AIAA - 2001 - 3068

Afterbody Heating Characteristics of a Proposed Mars Sample Return Orbiter

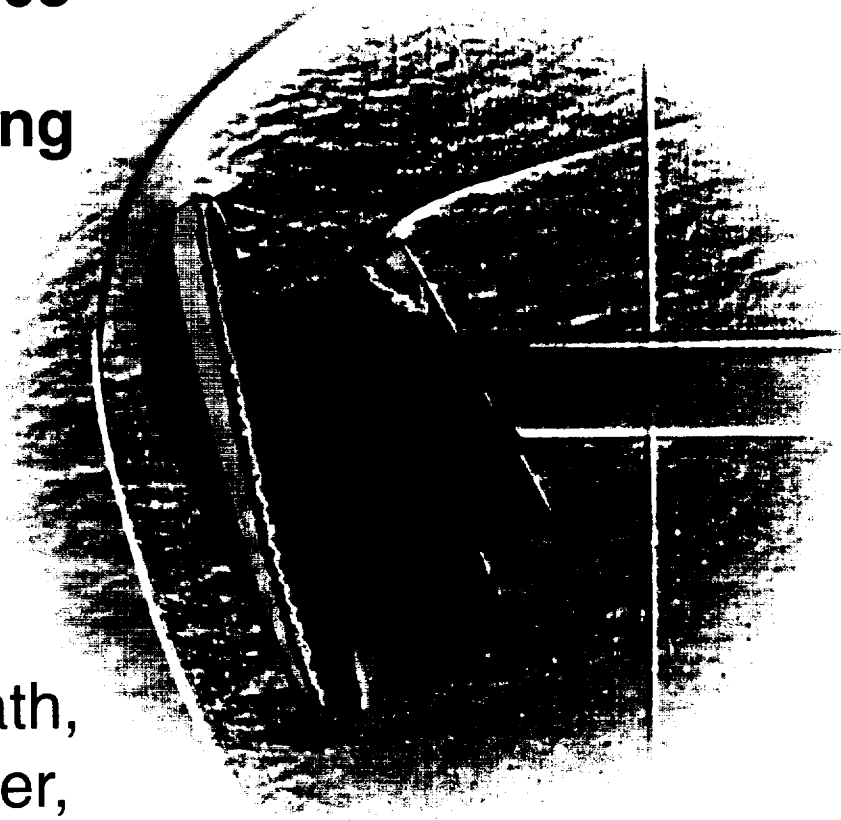

Thomas J. Horvath,
Nicholas C. Heiner,
Daniella M. Olguin,
F. McNeil Cheatwood and
Peter A. Gnoffo

NASA Langley Research Center
Hampton, Virginia 23681-2199

35th AIAA Thermophysics Conference

11-14 June 2001 / Anaheim, CA

AFTERBODY HEATING CHARACTERISTICS OF A PROPOSED MARS SAMPLE RETURN ORBITER

Thomas J. Horvath*, Nicholas C. Heiner**, Daniella M. Olguin**, F. McNeil Cheatwood*

and

Peter A. Gnoffo*
NASA Langley Research Center

Abstract

Aeroheating wind-tunnel tests were conducted on a 0.028 scale model of an orbiter concept considered for a possible Mars sample return mission. The primary experimental objectives were to characterize hypersonic near wake closure and determine if shear layer impingement would occur on the proposed orbiter afterbody at incidence angles necessary for a Martian aerocapture maneuver. Global heat transfer mappings, surface streamline patterns, and shock shapes were obtained in the NASA Langley 20-Inch Mach 6 Air and CF_4 Tunnels for post-normal shock Reynolds numbers (based on forebody diameter) ranging from 1,400 to 415,000, angles of attack ranging from -5 to 10 degrees at 0, 3, and 6 degree sideslip, and normal-shock density ratios of 5 and 12. Laminar, transitional, and turbulent shear layer impingement on the cylindrical afterbody was inferred from the measurements and resulted in a localized heating maximum that ranged from 40 to 75 percent of the reference forebody stagnation point heating. Comparison of laminar heating prediction to experimental measurement along the orbiter afterbody highlight grid alignment challenges associated with numerical simulation of three-dimensional separated wake flows.

Nomenclature

D	aerobrake base diameter (in)
d	diameter (in)
h	heat transfer coeff. (lbm/ft^2-sec), $q/(H_{aw} - H_w)$ where $H_{aw} = H_{t,2}$
H	enthalpy (BTU/lbm)
M	Mach number
P	pressure (psia)
q	heat transfer rate (BTU/ft^2-sec)
R	radius (in)
Re	unit Reynolds number (1/ft)
t	time (sec)
T	temperature (°F)
x	axial distance along cylinder afterbody (in)
α	angle of attack (deg)
ϕ	cone half angle (deg)
θ	shear layer turning angle (deg)
ρ	density (lbm/in^3)
γ	ratio of specific heats

Subscripts

aft	vehicle afterbody
eff	angular dimension relative to a vector normal to base plane of aerobrake
f	forebody
l	local condition
∞	free-stream conditions
n	model nose
ref	theoretical reference stagnation point heating
s	surface quantity, support sting
t, 1	reservoir conditions
2	stagnation conditions behind normal shock
w	wall

Introduction

As the result of a restructured[1-3] strategy for the exploration of Mars, it is anticipated that future robotic missions to Mars will continue to gather scientific data and demonstrate technologies required to address the feasibility of eventually establishing a human presence on Mars. The revised exploration architecture calls for a sample return opportunity as early as 2011[4]. A Mars sample return (MSR) mission would collect terrestrial material from the planet surface and return these samples to Earth for detailed analysis. Although missions designed to return samples from Mars have been considered in the past[5-7], all planetary environmental and surface sample data to date has been acquired from remote based measurements obtained from the surface or in orbit of Mars. An MSR round-

* Aerospace Technologist, NASA Langley Research Center, Hampton, VA.

** Cooperative education student, NASA Langley Research Center, Hampton, VA.

trip mission could require technologies such as aerocapture, precision landing, remote-controlled surface operations including surface material collection, orbital rendezvous, docking and sample transfer (all at Mars) culminating with a direct entry return at Earth (or shuttle rendezvous).

Prior to the revised Mars exploration architecture, one approach considered for sample return called for a joint US/European MSR mission[8-11]. Key elements of this mission profile are highlighted in Fig. 1. Collected surface samples would be placed into Mars orbit in advance of the arrival of a second vehicle, a French designed MSR orbiter (MSRO)[12]. Upon planetary approach, the MSRO vehicle would perform an aerocapture maneuver in the Martian atmosphere. With aerocapture, deceleration and orbital insertion is accomplished aerodynamically (in contrast to traditional propulsive techniques) using a blunt aeroshell. After an orbital rendezvous, the material samples would be autonomously transferred to the MSRO and stored in the US-designed Earth Entry Vehicle[8] (EEV) for the return transit to earth.

The EEV and the retrieval hardware on the MSRO would reside behind the aeroshell during the aerocapture maneuver prior to its jettison. Proper positioning of this hardware is essential to insure aerodynamic stability of the MSRO during aerocapture, to reduce the chances of biological contamination of the EEV(s), and to avoid thermal damage from localized near wake phenomenon. Although it is generally recognized that convective heating rates to payloads behind aerobrakes are low[13], localized heating maximum can occur if the boundary layer that separates from the shoulder of the aeroshell impinges on the afterbody[14-17]. The complexity of hypersonic blunt body base flow is shown schematically in Fig. 2.

The purpose of the present study was to experimentally investigate the near wake closure characteristics of a proposed MSRO vehicle. The primary objective was to experimentally determine if flow impingement occurred on the MSRO afterbody, and if present, determine the location and magnitude of the heating peak for comparison of prediction to measurement. Prediction methods that accurately model the near wake characteristics of blunt bodies are desired to reduce conservative design margins for planetary entry vehicles.

Initial tests in the Langley 20-Inch Mach 6 CF_4 Tunnel were used to assess laminar MSRO wake closure characteristics because of the facility's ability to provide normal shock density ratios (ρ_2/ρ_∞) of the same magnitude as that incurred in flight. It is anticipated that entry of the MSRO into the atmosphere of Mars (continuum-flow regime) during the aerocapture maneuver will produce values of shock density ratio near 20 (these high values of normal shock density ratio encountered in hypervelocity flight are produced from dissociation of atmospheric gases as they cross through the shock wave into the shock layer and are often referred to as real gas effects). Flight values of normal shock density ratio are significantly larger (3 to 4 times) than those produced in conventional blowdown hypersonic wind tunnels using air or nitrogen as a test gas[18]. The NASA Langley 20-Inch Mach 6 CF_4 Tunnel utilizes a test gas (tetrafluoromethane-CF_4) with a molecular weight 3 times that of air in order to generate a normal shock density ratio of 12 thereby simulating this particular aspect of a real gas. The simulation is achieved at moderate levels of enthalpy and without dissociation of the test gas. It is well recognized the normal shock density ratio is one of the primary flight simulation parameters that govern the inviscid flow and aerodynamics of blunt bodies at hypersonic speeds[19]. Complimentary tests in a perfect gas Mach 6 air facility were later performed over a larger Reynolds number range to assess the effects of shear layer transition on wake closure and impingement heating.

The MSRO was tested at normal shock density ratios of 12 and 5 (in CF_4 and air, respectively) over a range of freestream unit Reynolds number from 1.2×10^4 to 8×10^6 per foot (post shock Reynolds number range based on aeroshell diameter of 1,400 to 415,000). Angle of attack was varied from -5 deg to 10 deg at zero deg sideslip (limited data at 3 and 6 deg sideslip). Test techniques that were utilized during these tests include thermographic phosphors, which provided global quantitative surface heating images; oil-flow, which provided surface streamline information; and schlieren, which provided shock system details. Emphasis was placed on the afterbody surface heating augmentation due to shear layer impingement.

Experimental Methods

Model

The Outer Mold Lines (OML) of the proposed MSRO vehicle shown in Fig. 3 represents a reference baseline concept for which experimental and computational wake assessment studies can be conducted. The proposed MSRO vehicle consists of a drag brake and a base-mounted cylindrical afterbody (d_{aft}/d_f=0.48). The base of the drag brake (aeroshell) is concave inwards as shown in Fig. 3. A single EEV for sample storage and a housing structure for the retrieval/transfer hardware are positioned on the afterbody. The drag brake, or aeroshell, is based upon a design originally proposed in support of the Aeroassist Flight Experiment (AFE)[20] – a 60 degree elliptically blunted cone with the base raked at a 73 degree angle. At zero degrees angle of attack, the wind vector is aligned with the minor axis of the ellipsoidal nose (see Fig. 3).

A photograph of two 4-in. diameter (0.028 scale) cast ceramic MSRO models used in the test is shown in Fig. 4. For construction of the fused silica models, a rapid prototyping technique was utilized. Stereolithography (SLA) was used to build a resin aeroshell model with various, detachable SLA afterbodies representing a component buildup of the return orbiter EEV and retrieval/transfer housing structure. The SLA resin aeroshell was then assembled with the desired afterbody; the mated pair served as a pattern to construct molds from which the cast ceramic MSRO models were made. A support sting enters from the rear of the cylindrical afterbody. A magnesia ceramic was used to backfill the cylindrical afterbody, thus providing strength and support to the sting support structure. The aeroshell baseplanes on the MSRO models were constructed both open (concave inwards as sketched in Fig. 3) and closed. A photograph of these two base configurations is shown in Fig. 4.

Typically, two casts of each configuration are made; the primary being immediately prepared for testing and the back-up shell held in reserve, in the event of problems with the primary. In order to obtain accurate heat transfer data with the phosphor technique, the models are cast with a material having low thermal diffusivity and well defined, uniform, isotropic thermal properties. The phosphor coatings typically do not require refurbishment between runs in the wind tunnel and have been measured to be approximately 0.001 inches thick. Details concerning the ceramic model fabrication technique and phosphor coating can be found in Refs. 21 and 22. Fiducial marks were placed on the model surface to assist in determining spatial locations accurately.

Once the phosphor testing was completed, the untested backup ceramic models were used for visualization tests (oil-flow and schlieren).

<u>Facility Descriptions</u>

Tests were conducted in two facilities managed under the Aerothermodynamic Facilities Complex (AFC). This complex presently consists of four hypersonic wind tunnels that represent a large fraction of the nation's conventional aerothermodynamic test capability[23]. Collectively, they provide a wide range of Mach number, unit Reynolds number, and normal shock density ratio. This range of hypersonic simulation parameters is due, in part, to the use of two different test gases (air and tetraflouromethane), thereby making the facilities unique national assets. The AFC facilities are relatively small and economical to operate, hence ideally suited for fast-paced aerodynamic performance and aeroheating, and transition studies aimed at screening, assessing, optimizing, and bench-marking (when combined with computational fluid dynamics) advanced aerospace vehicle concepts and basic fundamental flow physics research.

20-Inch Mach 6 Air Tunnel: Heated, dried, and filtered air is used as the test gas. Typical calibrated operating conditions for the tunnel are: stagnation pressures ranging from 30 to 500 psia; stagnation temperatures from 760 to 1000-degree R; and freestream unit Reynolds numbers from 0.5 to 8 million per foot. A two-dimensional, contoured nozzle is used to provide nominal freestream Mach numbers from 5.8 to 6.1. The test section is 20.5 by 20 inches; the nozzle throat is 0.399 by 20.5-inch. A bottom-mounted model injection system can insert models from a sheltered position to the tunnel centerline in less than 0.5-sec. For the transient heat transfer tests, the model residence time in the flow was limited to 5 seconds. A detailed description of this facility may be found in Ref. 23.

Mach 6 CF_4 Tunnel : Heated, dried, and filtered tetrafluoromethane (CF_4) is used as the test gas. Typical calibrated operating conditions for the tunnel are: stagnation pressures ranging from 85 to 2000 psia, stagnation temperatures up to 1300-degree R, and freestream unit Reynolds numbers from 0.01 to 0.41 million per foot. A contoured axisymmetric nozzle is used to provide nominal freestream Mach numbers from 5.9 to 6.2. The nozzle exit diameter is 20 inches with the flow exhausting into an open jet test section; the nozzle throat diameter is 0.466-inch. A bottom-mounted model injection system can inject models from a sheltered position to the tunnel centerline in less than 0.5-sec. For the transient heat transfer tests, the model residence time in the flow was limited to 5 seconds. A detailed description of this facility may be found in Ref. 19.

<u>Test Conditions and Setup</u>

Nominal reservoir and corresponding free stream flow conditions for the MSRO test series are presented in Table 1. The freestream properties were determined from the measured reservoir pressure and temperature and the measured pitot pressure at the test section. Static pressure in the CF_4 test section that enclosed the open jet were monitored to assess the potential for contraction of the open-jet test core flow with time during any given run. The ratio of pitot to reservoir pressure was also measured in both facilities during each run to determine flow conditions and test times. The ratio of projected model frontal area to core flow cross sectional area for the 0.028-scale model is approximately 0.15.

All models were supported by a cylindrical steel rod (sting) which extended downstream from the model base at a 105-degree incidence angle relative to the forebody base plane. This was done to align the sting along a computationally predicted wake axis with the model at zero degree incidence. To determine the sensitivity of the support system on base flow heating, several runs were made with an adapter sleeve placed over the existing sting which increased the sting to forebody diameter ratio (d_s/d_f) from 0.19 to 0.32. Model angle-of-attack and sideslip were set to zero in the tunnel using a combination of an inclinometer and a laser alignment system. A photograph of the installation in the CF_4 tunnel is shown in Fig. 5.

Test Techniques

Global Phosphor Thermography: Advances in image processing technology which have occurred in recent years have made digital optical measurement techniques practical in the wind tunnel. One such optical acquisition method is two-color relative-intensity phosphor thermography[24-26] which has been utilized in several aeroheating tests conducted in the hypersonic wind tunnels of NASA Langley Research Center.[27-30]. With this technique, ceramic wind tunnel models are fabricated and coated with phosphors that fluoresce in two regions of the visible spectrum when illuminated with ultraviolet light. The fluorescence intensity is dependent upon the amount of incident ultraviolet light and the local surface temperature of the phosphors. By acquiring fluorescence intensity images with a color video camera of an illuminated phosphor model exposed to flow in a wind tunnel, surface temperature mappings can be calculated on the portions of the model that are in the field of view of the camera. A temperature calibration of the system conducted prior to the study provides the look-up tables that are used to convert the ratio of the green and red intensity images to global temperature mappings. With temperature images acquired at different times in a wind tunnel run, global heat transfer images are computed assuming one-dimensional semi-infinite heat conduction. The primary advantage of the phosphor technique is the global resolution of the quantitative heat transfer data. Such data can be used to identify the heating footprint of complex, three-dimensional flow phenomena (e.g., separation/reattachment, transition fronts, turbulent wedges, boundary layer vortices, etc.) that are extremely difficult to resolve by discrete measurement techniques. Because models are fabricated and instrumented more rapidly and economically, global phosphor thermography has largely replaced discrete heating instrumentation in Langley's AFC.

Schlieren photography: Flow visualization in the form of schlieren was used to complement the surface temperature and heating measurements. The LaRC 20-Inch Mach 6 Air and CF_4 Tunnels are equipped with a pulsed white-light, Z-pattern, single-pass schlieren system with a field of view encompassing the entire test core. The light sources are pulsed for approximately a 3 ms. Images were recorded on a high-resolution digital camera and enhanced with commercial software.

Oil Flow Visualization: Surface streamline patterns were obtained using the oil-flow technique. Backup ceramic models were spray-painted black to enhance contrast with the white pigmented oils used to trace streamline movement. A thin basecoat of clear silicon oil was first applied to the surface, and then a mist of pinhead-sized pigmented-oil drops was applied onto the surface. After the model surface was prepared, the model was injected into the hypersonic flow, and the development of the surface streamlines was recorded with a conventional video camera. The model was retracted immediately following flow establishment (and formation of streamline patterns) and post-run digital photographs were taken.

Data Reduction and Uncertainty

A 16-bit analog-to-digital facility acquisition system was used to acquire flow condition data. Measured values of $P_{t,1}$ and $T_{t,1}$ are believed to be accurate to within ±2 percent.

Heating rates were calculated from the global surface temperature measurements using one-dimensional semi-infinite solid heat-conduction equations, (see Ref. 26). As discussed in Ref. 26, the accuracy of the phosphor system measurement is dependent on the temperature rise on the surface of the model. For the heating measurements, the phosphor system measurement accuracy is believed to be better than ±8%, and the overall experimental uncertainty of the phosphor heating data due to all factors is estimated to be ±15%. In areas on the model where the surface temperature rise is only a few degrees (i.e. cylinder afterbody, upstream of flow reattachment), the estimated overall uncertainty is on the order of ±25%. Repeatability for the normalized centerline (laminar) heat transfer measurements on the afterbody was found to be generally better than ±8%. Uncertainties in model angle-of-attack and sideslip are believed to be ±0.2 degree.

Computational Methods

The Langley Aerothermodynamic Upwind Relaxation Algorithm (LAURA)[31,32] was used to provide laminar numerical simulations of the MSRO wake structure at M_∞=6 CF_4 wind tunnel conditions. Grid topology, sensitivity studies, and convergence metrics are discussed in Ref. 11. On the surface, no-slip conditions were applied and model wall temperature was assumed isothermal and set to 80 deg F (T_w/T_t=0.43).

Results and Discussion

Preface

The heating mappings and distributions in the subsequent sections are presented in the form of a normalized heating coefficient, h/h_{ref} where h_{ref} corresponds to the theoretical stagnation point heating at α=0 degrees on the model forebody using the method of Ref.33. The reference radius is 1.81-inches, which approximates the ellipsoidal nose radius of the AFE forebody in the model plane of symmetry. For the global images, the colors tending towards red indicate areas of higher heating (temperatures) while the colors towards blue represent regions of lower heating. Shear layer turning angle, which is measured relative to a direction normal to the base plane of the aerobrake (see Fig. 3), is inferred from schlieren images, surface streamline patterns, and local heating. Unless indicated otherwise, all data presented was obtained on models with the aeroshell baseplane configured as open (see Fig. 4).

Shear layer Identification

The MSRO is intended to trim between α=-4 and +4 degrees during its aerocapture maneuver at Mars. Schlieren images associated with the MSRO flow field (in M_∞=6 air at Re_{2D}=4.15 x 10^5) are presented in Fig. 6, for a range of angle of attack ($-5<\alpha<+10$ degrees). In the sequence of images, a weak lip shock associated with the rapid over expansion and subsequent recompression around the aerobrake shoulder is evident, in addition to a relatively thin free shear layer. While not attempted in the present study, M_∞=6 air flow field surveys in the base region of a similar blunt body[14] have correlated wake lip shock and shear layer boundaries inferred from pitot pressure profiles to visual locations inferred from schlieren images. The MSRO schlieren images shown in Fig. 6, indicate that at angles of attack larger than +6 degrees, the afterbody upper symmetry plane (surface opposite the EEV and retrieval hardware) avoids direct shear layer impingement for this condition. As the model angle of attack is decreased, the onset of shear layer impingement is observed to occur (in air) between α=+6 and +5 degrees, and is indicated by a weak recompression shock at the reattachment point near the end of the cylindrical afterbody. The shear layer impingement point progressively moves towards the aerobrake base (and the strength of the recompression shock increases) as the vehicle angle of attack is decreased to α=-5 degrees. At the limiting incidence angle of α=-5 degrees, an interaction of the lip shock with the afterbody recompression shock is observed near the aft corner of the afterbody. Shear layer impingement on the EEV and retrieval hardware are not observed in M_∞=6 air for $-5<\alpha<+10$ degrees. The sensitivity of the schlieren system is insufficient to detect the wake shear layer in the CF4 facility due to the low density of the base region flow.

Heating distributions obtained in M_∞=6 air and CF_4 along the cylinder afterbody at several time intervals are used to determine when the base flow is established. Although some degree of wake flow unsteadiness is inherent, the shear layer position is typically stable within the framing rate (30 frames/sec.) and spatial resolution of the schlieren video imagery.

Shear layer Impingement

Shear layer impingement will result in localized surface pressure and convective heating increases. Typical surface streamlines and heating distributions on the MSRO afterbody in the presence of shear layer impingement are shown in Figs. 7 and 8 at α=-4 degrees for M_∞=6 air and Re_{2D}=6.5 x 10^4. Similar trends were observed at corresponding conditions in M_∞=6 CF_4. The pressure rise due to reattachment and downstream recompression contributed to the reversal of the flow back towards the open forebody base as inferred from the surface streamline patterns (see Fig.7). The location of the dividing streamline delineating the entrained recirculating base flow from the flow continuing downstream is evident in this figure. As discussed in a subsequent section, this reversed flow was often observed to produce complex recirculation patterns on the forebody base presumably due to primary and secondary vortices. The corresponding surface heating (see Fig.8), indicates that the local impingement heating at this condition approached 65% of the reference forebody stagnation point value; heating levels upstream of the attachment location and on the base were under 5% of the reference stagnation value. Regions of flow reattachment inferred from heating patterns on the afterbody side is not evident for sideslip angles up to 6 degrees (not shown).

MSRO afterbody wall temperatures in M_∞=6 air obtained 5 seconds after model exposure were generally uniform (T_w=110 deg. F; T_w/T_t=0.61) in locations away from impingement. At higher Reynolds numbers, localized turbulent heating near impingement produced wall temperatures as high as 230 degree. F (T_w/T_t=0.74) with peak heating levels that approached 75 % of the reference stagnation value.

Reynolds Number Effects

Because experimental evidence revealed shear layer impingement at trim angles of attack, it became necessary to quantify impingement heating levels and thus identify the state of the prevailing interaction (laminar, transitional, or turbulent). As discussed in detail in Ref. 34, separated flows are largely characterized by the prevailing boundary layer or shear layer state. Differences in laminar and turbulent separated regions are primarily attributed to enhanced mixing (greater effective momentum transfer) associated with turbulence. The presence of a transitional shear layer often leads to much higher peak heating at reattachment than if the separated flow is entirely laminar or turbulent[14,35]. While edge conditions (M, Re, and γ) at the point of boundary layer separation determine the initial shear layer turning angle, the state of the interaction (reattachment) downstream also effects the extent (and degree) of unsteadiness of the reversed flow. Thus, a secondary objective of the experimental program was to produce both a laminar and turbulent interaction from which comparisons to numerical solutions could be made. Confidence levels associated with numerical simulation of separated laminar flows are generally lower than for laminar attached flows. The additional complexity of accurately modeling transitional or turbulent separated flow has also proven to be a challenge[36] (ironically, it is the laminar wake interaction that is often difficult to achieve in conventional ground based hypersonic wind tunnel due to facility operational limitations at low Reynolds numbers).

The M_∞=6 CF_4 tunnel was initially attractive from the perspective of testing in a gas with a low ratio of specific heats (γ) - as is encountered in hypervelocity flight. In addition, the facility provides the best opportunity from which to maintain a laminar interaction since it operates at low pressures (and hence, Reynolds numbers). Normalized heating along the MSRO cylindrical afterbody is shown in Fig. 9 at α=-4 degrees for M_∞=6 CF_4 over a range of post normal shock Reynolds numbers (Re_{2D}=1,420 to 52,442). The abscissa of Fig. 9 (and all subsequent afterbody heating distributions) refers to the running length along the cylinder non-dimensionalized by the forebody diameter, originating at the aft corner and running forward towards the aerobrake base. The relatively small invariance in the measured magnitude and spatial location of the reattachment heating peak for Re_{2D}=1,420 to 3,946 is interpreted as evidence of a laminar interaction. An increase (and subsequent movement) of peak reattachment heating towards the aerobrake base for Re_{2D}>3,946 suggested a non-laminar interaction[14,16,37] and/or an increase in the shear layer turning angle. The effects of Reynolds number on shear layer turning angle will be discussed in a subsequent section.

The M_∞=6 air tunnel provides a two order-of-magnitude increase in post-normal shock Reynolds number over the CF_4 data. Normalized heating along the MSRO cylindrical afterbody is shown in Fig. 10 at α=-4 degrees in M_∞=6 air for Re_{2D}=36,700 to 415,000. A small overlap in terms of post-normal shock Reynolds number exists between the two facilities. Qualitatively, the magnitude of the measured impingement heating peak in M_∞=6 air at the lowest Reynolds number (Re_{2D}=36,700- Fig. 10) is consistent with that measured at the highest Reynolds number (Re_{2D}=52,442-Fig. 9) in M_∞=6 CF_4. The continuation of the forward movement of the local reattachment heating peak in M_∞=6 air toward the aerobrake base is evident. The continual rise in the heating peak to h/h_{ref}=0.66, as measured at Re_{2D}=65,000 and the subsequent drop to h/h_{ref}=0.60 for Re_{2D}=123,000, (see Fig. 10), is interpreted as the condition at which the transitional shear becomes fully turbulent. It is suggested that this situation is analogous to the transitional "overshoot" phenomenon commonly observed with attached wall boundary layers (where it has been conjectured that the larger vortical length scales associated with transitional flows are more effective at momentum transfer than the finer scales found in a fully turbulent situation). In the postulated turbulent regime, a linear rise in the non-dimensional heating peak to 0.73 for Re_{2D}=415,000 was measured in M_∞=6 air. A Reynolds number collapse of turbulent heating data is not observed when normalized with a laminar reference value.

The approximate range of Re_{2D} at which the wake interaction has been postulated to go from a laminar to a transitional state, and from a transitional state to a fully turbulent are presented in Fig. 11. In this figure, the local heating peak at reattachment has been plotted as a function of Re_{2D} for both M_∞=6 air and CF_4. As inferred in Fig. 9, the relatively small invariance in the measured magnitude of the reattachment heating peak for Re_{2D}=1,420 to 3,946 was interpreted as evidence of a laminar interaction in M_∞=6 CF_4.

A limited literature search yielded several empirically derived correlations from which to determine the onset of wake flow transition. In a qualitative attempt to classify the present M_∞=6 CF_4 results as laminar, the data are presented in terms of, (and compared against), a simple unified wake transition correlation[38], Fig. 12. The parameters for the original correlation in Ref. 38 are freestream length Reynolds number (the length based upon the axial wake transition location relative to the base) and freestream Mach number. The correlation was developed from a large experimental database for cones, spheres, wedges, and sphere-cones that were tested over a range of supersonic and hypersonic Mach numbers. The potential effects of bluntness and body shape on wake transition were recognized in Ref. 38 and the length Reynolds number parameter was modified to include the square of the ratio of the freestream Mach number to a local wake Mach number. In terms of the correlation, the present M_∞=6 CF_4 condition (interpreted as laminar for Re_{2D}=1,420) is an order of magnitude or more below the specified criteria for wake transition. The local wake Mach number for the present results was determined from laminar prediction corresponding to a location just outside of the recirculating base flow (near shear layer impingement). The size of the symbols, (Fig. 12), are indicative of the dependence of the correlation parameter to the variation in Mach number as computed in this region. The transition length was assumed to be the axial distance of the aft cylinder (presumably where transition was observed) to the MSRO base. The M_∞=6 CF_4 results which were interpreted as transitional (Re_{2D}=52,442) were significantly closer to the correlation criteria for wake transition.

Base Effects

It is generally recognized that the presence of a support sting will have an effect on the base flow characteristics of a blunt body in hypersonic flow. A limited data set was taken to assess support interference effects. Experimentally, the sensitivity of the MSRO afterbody heating to the potential effects of a cylindrical model support sting was assessed for sting-to-model forebody diameter ratios (d_s/d_f) of 0.19 and 0.32. Fig. 13 shows that at a transitional Reynolds number (Re_{2D}=36,700), for M_∞=6 air at α=-4 degrees, an increase in the support sting diameter produces no measurable effect. Transitional data for M_∞=6 CF_4 (not shown) supports a similar conclusion. Comparison of the data in Fig. 13 also serves to indicate the level of repeatability associated with the wake heating measurements.

As shown in Figs. 14, 15, and 16, the state of the near wake (laminar, transitional, and turbulent respectively) has a pronounced effect on the magnitude of the peak heating associated with shear layer impingement for MSRO models (both open and closed baseplanes-see Fig. 4). For a laminar wake condition (Re_{2D}=3,946) in M_∞=6 CF_4 at α=-4 degrees, the closed (or filled baseplane) appeares to alter the base flow and lower the afterbody peak heating relative to that obtained with the open base by approximately 60% (from h/h_{ref}=0.43 to 0.27), Fig. 14. In contrast, a turbulent wake condition (Re_{2D}=415,000) in M_∞=6 air increases afterbody peak heating for the closed baseplane by approximately 23% (from h/h_{ref}=0.73 to 0.90), Fig. 16. Evidence of the complexity of the turbulent reversed flow impingement onto the closed baseplane at M_∞=6 air (Re_{2D}=415,000) is shown in the surface streamline patterns in Fig. 17. Baseplane surface heating in this vicinity (not shown) is approximately h/h_{ref}=0.12. When the shear layer state is interpreted as transitional in M_∞=6 air (Re_{2D}=52,442), no changes in peak heating magnitude or location for the open and closed baseplanes is observed, Fig. 15 (a similar conclusion was obtained for transitional measurements in M_∞=6 CF_4- not shown). Thus, the turbulent wake associated with the closed MSRO base represents a worst case scenario in terms of afterbody heating where localized values at reattachment approached forebody stagnation levels.

Shear layer Turning Angle Characteristics

From a practical perspective, the usable volume for payload placement behind an aerobrake is generally constrained by the position of the wake free shear layer. The wake boundaries from which the MSRO afterbody was initially designed were inferred from a correlation derived from a series of ground-based blunt body tests at M_∞=6 and 10 air and numerical flight prediction[39]. In this correlation, measured and computed shear layer deflection angles and vehicle angle of attack are expressed relative to a direction normal to the given aerobrake baseplane. A linear relationship was identified between the shear layer turning angle (θ_{eff}) and the effective angle of attack (α_{eff}).

The shear layer turning angle (as a function of effective angle of attack) inferred from the present heating, surface streamline, and shock pattern measurements in M_∞=6 air and CF_4 are presented in Fig. 18 and Fig. 19, respectively. For clarification purposes, the ground based results from Ref. 39 are presented in these figures in the form of a shaded band. Consistent with the methodology of Ref. 39, the shear layer deflection angles are measured relative to a straight line drawn from the model base corner to the measured location of the attachment point as inferred from surface streamline patterns, schlieren images, and the location of peak heating using phosphor thermography.

The present MSRO results obtained with the open base plane exhibit the same general linear trend as the correlation of Ref. 39. The turning angle inferred from the CF_4 heating and streamline measurements (see Fig. 19), compare well with the correlation. In the present data, the variation of the turning angle for each effective angle of attack has been attributed to transitional/turbulent Reynolds number effects discussed earlier. That is, for a non-laminar interaction, an increase in Reynolds number moves the impingement location towards the aerobrake base, implying a larger turning angle. The effect of Reynolds number on shear layer turning for a laminar interaction is inconclusive due to the limited range of Reynolds number for laminar CF_4 data. The M_∞=6 air results, Fig. 18, indicate a bias towards a larger turning angle relative to the original correlation and this is, in part, attributed to the greater turbulent Reynolds number range achieved in the present tests.

For a given Re_{2D} corresponding to a non-laminar shear layer, the shear layer turning angle as inferred from surface streamlines or shock patterns is generally greater than that determined via the peak heating location. Shear layer turning angles as a function of Re_{2D} for α=-4 degrees in M_∞=6 air and CF_4 are presented in Fig. 20 and Fig. 21, respectively. For the laminar M_∞=6 CF_4 condition (Re_{2D}=1,420 to 3,946), the turning angle associated with peak heating on the afterbody is within one degree of that inferred from surface streamlines or shock patterns, as shown in Fig. 21. For transitional/turbulent conditions in M_∞=6 air (Re_{2D}> 3,946, Fig. 20), this difference is as large as four degrees. As indicated by the data in Figs. 20 and 21, the turning angle for a transitional/turbulent interaction is larger than its laminar counterpart. As inferred from this data, the transitional/turbulent heating maximum on the cylinder afterbody (Re_{2D}>3,946) is located downstream of the reattachment point as determined from surface streamlines or shock patterns.

It was concluded in Ref. 39 that no significant effects due to M_∞, Re_{2D}, or vehicle forebody geometry were observed in the ground-based test data that the shear layer turning angle correlation was derived from. Slightly larger shear layer turning angles were predicted at flight conditions and it was suggested that this could have been a gas chemistry effect. As discussed in Ref. 39, the severe compression in the forebody shock layer and the subsequent rapid expansion into the wake are characterized by high temperature, thermo-chemical nonequilibrium processes. In contrast to quantifying the aerodynamic effects associated a real gas, the applicability of the present MSRO simulation tests in

CF_4 are not certain regarding the characterization of blunt body wake flow. From an aerodynamic perspective, it has been shown[40] that the increments and trends provided by real gas simulation tests in air and CF_4 are applicable to flight provided that (1) the vehicle aerodynamics are dominated by the windward surface pressure (shear stress contributions negligible), (2) γ within the flight windward shock layer does not significantly vary spatially, and (3) γ within the flight windward shock layer is close in magnitude to that produced in CF_4 (γ=1.1). Despite ground based testing simulation issues and geometrical afterbody differences from those configurations used to define the turning angle correlation of Ref. 39, the present MSRO laminar CF_4 data has suggested the general applicability of the correlation for predicting wake shear layer turning for initial design estimates. If shear layer transition in flight is anticipated (i.e. via forebody ablation or surface roughness) a larger turning angle should be expected.

The intent of the baseline MSRO afterbody design was to avoid impingement at trim angles of attack. The present results along with recent hypersonic tests[12,41] conducted in European facilities (in air and CO_2) have all indicated flow impingement on the MSRO afterbody near trim conditions. Flight computations[10-12] have indicated impingement as well. These experimental and computational results reveal the presence of impingement which will necessitate the use of a supplemental thermal protection system such as an afterbody shield discussed in Ref. 12. In hindsight, it appears that the early engineering estimates of the MSRO wake closure characteristics (to avoid shear layer impingement) were not conservative enough. For design purposes, a shear layer turning angle of 30 degrees (see Fig. 19) was originally assumed based upon an effective angle of attack of 15 (α=+2 degrees) degrees. As aerodynamic performance of the aerobrake during an aeropass maneuver was refined to include dispersions, the effective angle of attack to trim the MSRO was increased to 19 degrees (α=-2 degrees) and later to 21 degrees (α=-4 degrees). Based upon the correlation of Ref. 39, the projected shear layer turning angle relative to the baseplane would increase to approximately 39 degrees. The relationship of these turning angles relative to the MSRO afterbody is shown, Fig. 22. As inferred from the correlation, impingement on the afterbody would occur for effective angles of attack of 19 and 21 degrees. A small rotation or lateral displacement of the afterbody in the plane of symmetry (or scarfing the aft corner) would possibly provide a means to avoid impingement. An afterbody shield would also serve to prevent impingement but would add undesirable mass to the orbiter.

Comparison to Measurement

Accurate, quantitative measurement and numerical simulation of laminar, transitional, and turbulent separated/reattaching flows remains a challenge. Due to the operating range of most continuum hypersonic facilities, maintaining a laminar shear layer in regions of strong expansion (such as that encountered in the near wakes of blunt bodies) has in the past proven difficult[14,15]. The influence of tunnel noise on shear layer transition is not well understood. When turbulent interactions are present, numerical turbulence models play a crucial role in the simulation of these non-laminar flows where separation, shock-boundary layer interaction, and flow reattachment are present[30]. For the simpler laminar interactions, which avoid turbulence modeling, grid issues related to resolving near wake flow features such as the free shear layer persist[16].

The present experiments were performed in an effort to provide benchmark data for complex laminar/turbulent separated flows. Comparison of laminar heating prediction (via the LAURA code) to experimental measurement along the MSRO afterbody near impingement is shown in Fig. 23, for M_∞=6 CF_4 (Re_{2D}= 3,946). Measurement and prediction correspond to an open base. As discussed previously, the abscissa of this figure refers to the running length along the cylinder non-dimensionalized by the forebody diameter, originating at the aft corner and running forward towards the aerobrake base. The laminar experimental results indicate an impingement heating peak of h/h_{ref}=0.41 at x/D=0.02 in close proximity to the afterbody corner. Numerical results obtained on both grids indicate a local heating spike at the afterbody corner (x/D=0) where there is a rapid thinning of the boundary layer (the spatial resolution of the thermography technique was insufficient to resolve a high gradient heating peak at this location), followed by a broad heating plateau (0.02<x/D<0.1) interpreted as shear layer reattachment. As indicated in Ref. 39, the original grid used in this numerical simulation was adapted from a mesh utilized for early flight predictions. This modified grid had finer resolution in the near wake relative to that used for the flight cases but no attempt was made to align the grid with the shear layer. Some degree of numerical diffusion of the shear layer was expected. The numerical heating spike at x/D=0.24 is grid induced (see Ref. 39 for details).

In an attempt to assess the sensitivity of wake closure characteristics and shear layer diffusion to grid alignment, a second calculation was made with the mesh realigned with wake streamlines. As anticipated, the realigned grid reduces the level of numerical shear layer diffusion and produces a sharper heating spike (h/h_{ref}=0.33) at impingement. The location of this heating maximum (x/D=0.12) occurs closer to the aerobrake base and further away from the experimental peak.

Recent calculation of the Knudsen number near flow separation at the MSRO shoulder (not shown) suggest that, locally, application of slip boundary conditions at the wall near flow separation may be required. If practical, a 3-D coupled CFD-DSMC solution method could also prove beneficial in resolving differences between measurement and prediction. The present numerical predictions were made in the absence of a support sting. Computations with the support hardware modeled would eliminate the uncertainty posed by this difference. In addition, comparison of the turbulent M_∞=6 air data to numerical prediction using a two equation turbulence model are being considered.

Concluding Remarks

The Langley 20-Inch Mach 6 Air and CF_4 Tunnels were used to assess the afterbody heating characteristics of a proposed Mars Sample Return Orbiter (MSRO). The Mach 6 CF_4 tunnel utilizes a heavy gas (tetrafluoromethane-CF_4) in order to generate a higher value of normal shock density ratio (than can be achieved in air tunnels) which is more appropriate to simulation of hypervelocity flight through planetary or earth atmospheres. The primary experimental objectives were to determine if shear layer impingement would occur on the orbiter afterbody at incidence angles appropriate to an aerocapture maneuver, and if present, determine the location and magnitude of the heating peak for comparison of CFD predictions to measurement. Global heat transfer mappings, surface streamline patterns, and shock shapes were obtained for post-normal shock Reynolds numbers (based on forebody diameter) ranging from 1,420 to 415,000, angles of attack ranging from -5 to 10 degrees at 0, 3, and 6 degree sideslip, and normal-shock density ratios of 5 and 12. Laminar, transitional, and turbulent shear layer impingement on the cylindrical afterbody resulted in a localized heating maximum that ranged from 40 to 75 percent of the reference forebody stagnation point heating.

The present MSRO laminar data is consistent with a previously developed correlation for blunt body wake shear layer turning and has suggested the general applicability of the correlation towards initial design estimates defining the usable volume for payload placement behind an aerobrake. If wake shear layer transition in flight is anticipated (ie. via forebody ablation or surface roughness) a larger shear layer turning angle should be expected.

Acknowledgments

Without the assistance of the following individuals, this work would not have been possible: Mark Cagle, Chris Glass, Joe Powers, Mike Powers, Mark Griffith, Steve Nevins, Gary Waynewright, and Ed Covington for model design, fabrication, and instrumentation; Melanie Lawhorne, Harry Stotler, Crystal Kellam, Al Garner, John Ellis, Grace Gleason, Rowland Hatten, and Steve Jones for wind tunnel support; Sheila Wright, Bert Senter and Mike Difulvio for data acquisition assistance; Scott Berry and Brian Hollis for analysis support; Steve Alter for CFD volume grid generation; and Richard Wheless for documentation assistance. The authors gratefully acknowledge their contributions and behind-the- scenes work.

References

1. Smith, B. A.: "Lander Development Paced By Mars Science Results," *Aviation Week & Space Technology*, June. 26, 2000, p. 63.

2. Pieri, D.: "Rebuilding the U.S. Mars Exploration Program," *Launchspace*, July/Aug., 2000, p. 27.

3. Smith, B. A.: "NASA Weighs Mission Options," *Aviation Week & Space Technology*, Dec. 11, 2000, p.54.

4. Taverna, M. A.: "Europe to have Major Sample Return Role" *Aviation Week & Space Technology*, Dec. 11, 2000, p.60.

5. Williams, S.D.: "A Preliminary TPS Design for MRSR-Aerobraking at Mars and at Earth," AIAA-90-0052, Jan., 1990.

6. Meyerson, R. E. and Cerimele, C. J.: "Aeroassist Vehicle Requirements for a Mars Rover/Sample Return Mission," AIAA-88-0303, Jan., 1988.

7. Gamble, J. D.: "JSC Pre-Phase-A Study Mars Rover Sample Return Mission Aerocapture, Entry, and Landing Element," JSC-23230, May., 1989.

8. Mitcheltree, R. A., Kellas, S., Dorsey, J. T., Desai, P. N. and Martin, C.J.: "A Passive Earth-Entry Capsule for Mars Sample Return," AIAA-98-2851, June, 1998.

9. Amundsen, R. M., Dec, J. A., Mitcheltree, R. A., Lindell, M. C., and Dillman, R. A.: "Preliminary Thermal Analysis of a Mars Sample Return Earth Entry Vehicle," AIAA-2000-2584, June, 2000.

10. Glass, C. E. and Gnoffo, P. A.: "A 3-D Coupled CFD-DSMC Solution Method With Application To the Mars Sample Return Orbiter," 22nd International Sym. On Rarified Gas Dynamics, July, 2000, paper 4003.

11. Gnoffo, P. A.: "Computational Aerothermodynamics in Aeroasist Applications," AIAA-2001-2632, June, 2001.

12. Chanetz, B.: "Study of the Mars Sample Return Orbiter in the Hypersonic Wind Tunnel R5Ch," Atmospheric Reentry Vehicles and Systems, Arcachon, France, March, 2001.

13. Gnoffo, P. A.: "Planetary-Entry Gas Dynamics," Annual Review of Fluid Mechanics, 1999, p.459-

494.

14. Horvath, T. J., McGinley, C. B. and Hannemann, K.: "Blunt Body Near Wake Flow Field at Mach 6," AIAA-96-1935, June 17-20, 1996.

15. Horvath, T. J. and Hannemann, K.: "Blunt Body Near Wake Flow Field at Mach 10," AIAA-97-0986, Jan. 6-9, 1997.

16. Hollis, B. R.: "Experimental and Computational Aerothermodynamics of a Mars Entry Vehicle," NASA CR 201633, Dec., 1996.

17. Wells, W. L.: "Measured and Predicted Aerodynamic Heating on a Cylinder In Wake of AFE Configuration at Incidence," AIAA-89-2162, 1989.

18. Jones, R. A. and Hunt, J. L.: "Use of Tetrafluoromethane to Simulate Real-Gas Effects on the Hypersonic Aerodynamics of Blunt Bodies," NASA TR R-312.

19. Midden, R. E. and Miller, C. G. III: "Description and Calibration of the Langley Hypersonic CF_4 Tunnel: A Facility for Simulating Low Gamma Flow as Occurs for a Real Gas," NASA TP 2384.

20. Cheatwood, F. M., DeJarnette, F.R. and Hamilton, H. H. II: "Geometrical Description for a Proposed Aeroassist Flight Experiment Vehicle," NASA TM-87714, July, 1986.

21. Buck, G. M. and Vasquez, P.: "An Investment Ceramic Slip-Casting Technique for Net-Form, Precision, Detailed Casting of Ceramic Models," U. S. Patent 5,266,252, November 30, 1993.

22. Merski, N. R.: "Global Aeroheating Wind-Tunnel Measurements Using Improved Two-Color Phosphor Thermography Method" *Journal of Spacecraft and Rockets*, Vol. 36, No. 2, 1998, pp. 160-170.

23. Miller, C. G.: "Langley Hypersonic Aerodynamic/Aerothermodynamic Testing Capabilities - Present and Future," AIAA Paper 90-1376, June 1990.

24. Buck, G. M.: "Automated Thermal Mapping Techniques Using Chromatic Image Analysis," NASA TM 101554, April 1989.

25. Merski, N. R.: "Reduction and Analysis of Phosphor Thermography Data With the IHEAT Software Package," AIAA-98-0712, Jan. 1998.

26. Merski, N. R.: "Global Aeroheating Wind-Tunnel Measurements Using Improved Two-Color Phosphor Thermography Method" *Journal of Spacecraft and Rockets*, Vol. 36, No. 2, 1998, pp. 160-170.

27. Berry, S. A., Bouslog, S. A., Brauckmann, G. J. and Caram, J. M.: "Shuttle Orbiter Experimental Boundary-Layer Transition Results with Isolated Roughness," *Journal of Spacecraft and Rockets*, Vol. 35, No. 3, 1998, pp. 241-248.

28. Horvath, T. J., Berry, S. A., Hollis, B.R., Liechty, D.S. and Merski, N. R.: "X-33 Experimental Aeroheating at Mach 6 Using Phosphor Thermography," AIAA-99-3558, June, 1999.

29. Berry, S. A., Horvath, T. J., DiFulvio, M., Glass, C. and Merski, N. R.: "X-34 Experimental Aeroheating at Mach 6 and 10," *Journal of Spacecraft and Rockets*, Vol. 36, No. 2, 1998, pp. 171-178.

30. Horvath, T. J., Berry, S. A., Merski, N. R. and Fitzgerald, S.M.: "X-38 Experimental Aerothermodynamics," AIAA-2000-2685, June 2000.

31. Gnoffo, P. A.: "An Upwind-Biased, Point-Implicit Relaxation Algorithm for Viscous Compressible Perfect Gas Flows," NASA TP 2953, Feb., 1990.

32. Cheatwood, F. M. and Gnoffo, P. A.: "User's Manual for the Langley Aerothermodynamic Upwind Relaxation Algorithm (LAURA)," NASA TM 4674, April, 1996.

33. Fay, J. A. and Riddell, F. R.: "Theory of Stagnation Point Heat Transfer in Dissociated Air," *Journal of Spacecraft and Rockets*, Vol. 25, No. 2, 1958.

34. Wuerer, J. E. and Clayton, F. I.: "Flow Separation in High-Speed Flight: A Review of the State-of-the-Art," Douglas Report SM-46429 April, 1965.

35. Baker, P. J. and Martin, B.W.: "Heat Tranfer in Supersonic Separated Flow Over a Two-Dimensional Backward Facing Step," *International Journal of Heat and Mass Transfer*, Vol. 9, 1966.

36. Nance, R.P. and Horvath, T. J.: "Transition and Turbulence Modeling for Blunt-Body Wake Flows," AIAA-97-2570, June 1997.

37. Berger, S. A.: Laminar Wakes. American Elsevier Publ., Inc., 1971.

38. Zeiberg, S. L.: "Transition Correlations for Hypersonic Wakes," *AIAA Journal*, Vol. 2, No. 3, 1964.

39. Gnoffo, P. A., Price, J. M. and Braun, R. D.:

"Computation of Near-Wake Aerobrake Flowfields," *Journal of Spacecraft and Rockets*, Vol. 29, No. 2, March-April, 1992.

40. Brauckmann, G. J., Paulson, J. W. and Weilmuenster, J. K.: "Experimental and Computational Analysis of the Space Shuttle Orbiter Hypersonic Pitch-Up Anomaly," AIAA Paper 94-0632, January 1994.

41. Giraud, S. P.: "Investigation of the MSRO Heat Flux Distribution at the VKI Longshot Facility" MARS-TN-MSRO-001-VKI, Feb., 2001.

Table 1. Nominal flow conditions

Re_∞/ft (x10^6)	$Re_{2,D}$	M_∞	Test gas	$P_{t,1}$(psi)	$T_{t,1}$(°R)	ρ_2/ρ_∞
0.69	36,700	5.8	air	34	862	5.23
1.23	65,000	5.9	air	64	879	5.24
2.34	123,000	5.9	air	130	902	5.25
3.32	173,567	5.9	air	186	900	5.26
4.54	235,967	6.0	air	256	900	5.27
6.19	325,000	6.0	air	372	931	5.27
8.00	415,000	6.0	air	480	926	5.27
0.01	1,420	6.2	CF_4	61	1266	12.1
0.02	2,510	6.0	CF_4	82	1255	11.9
0.03	3,946	6.0	CF_4	118	1238	11.9
0.13	15,727	5.9	CF_4	390	1210	11.7
0.23	30,200	5.8	CF_4	747	1281	11.8
0.36	44,000	5.9	CF_4	1073	1248	11.7
0.41	52,442	5.9	CF_4	1314	1277	11.8

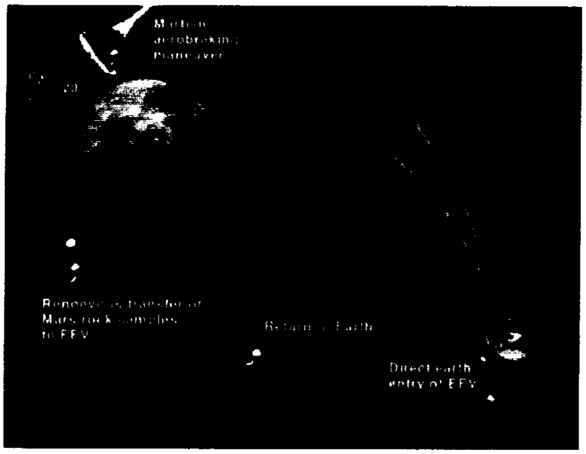

Figure 1. Major elements of a proposed Mars Sample Return (MSR) mission.

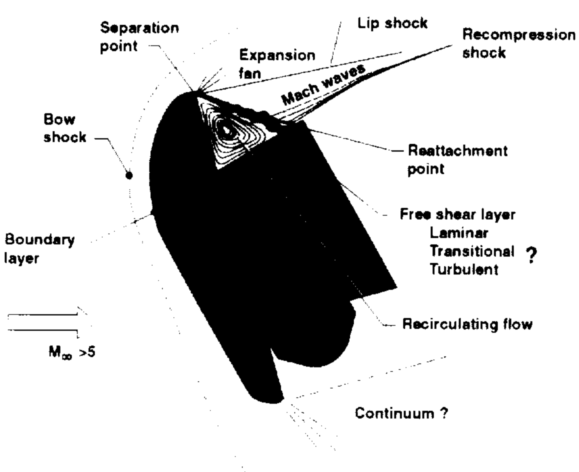

Figure 2. Schematic representation of the flow region behind a blunt body in hypersonic flow.

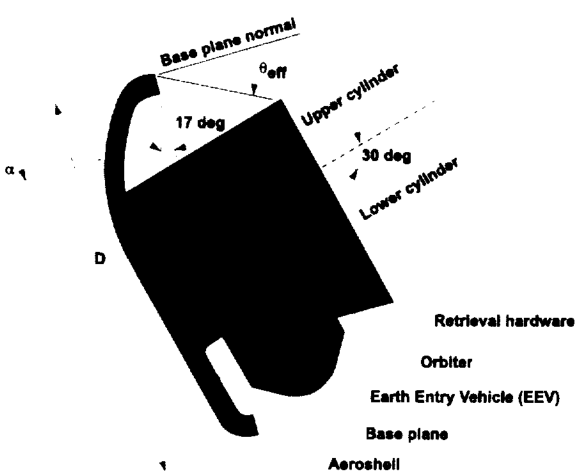

Figure 3. Sketch of the proposed Mars Sample Return Orbiter (MSRO).

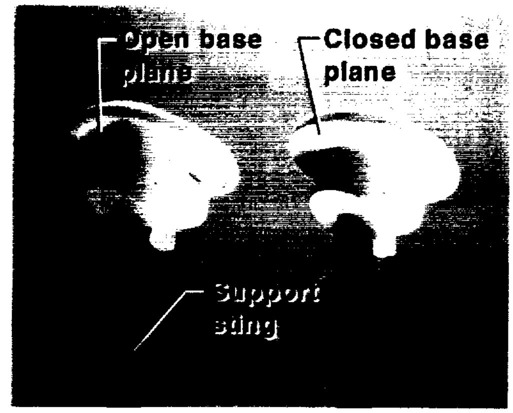

Figure 4. 0.028-scale MSRO ceramic heat transfer models.

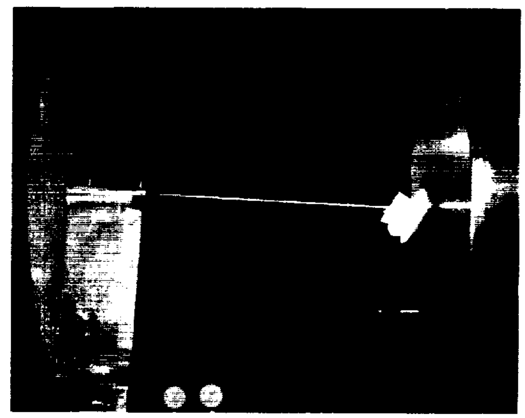

Figure 5. MSRO heating model installed in the NASA LaRC 20-Inch Mach 6 CF_4 tunnel.

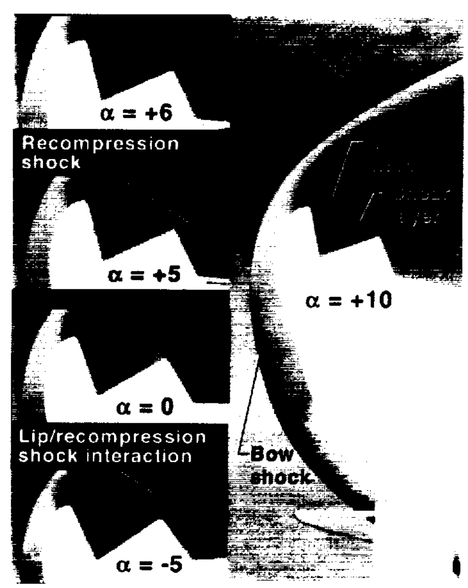

Figure 6. Schlieren images indicating general flow features observed from MSRO near wake flowfield. M_∞=6, air, Re_{2D}=415,000, $-5<\alpha<+10$ degrees.

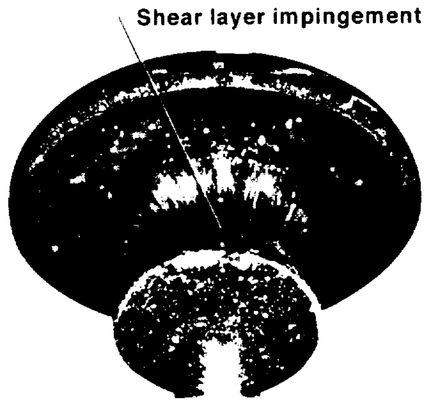

Figure 7. Typical surface streamlines on MSRO afterbody in the presence of shear layer impingement. M_∞=6, air, Re_{2D}=415,000, α= -4 degrees.

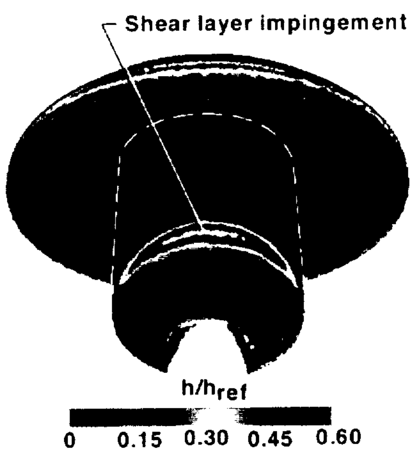

Figure 8. Typical surface heating on MSRO afterbody in the presence of shear layer impingement. M_∞=6, air, Re_{2D}=415,000, α= -4 degrees.

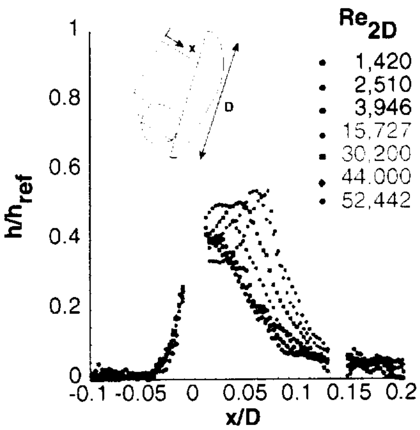

Figure 9. Effect of Reynolds number on normalized impingement zone heating along MSRO afterbody. M_∞=6, CF_4, ρ_2/ρ_∞=12, α= -4 degrees.

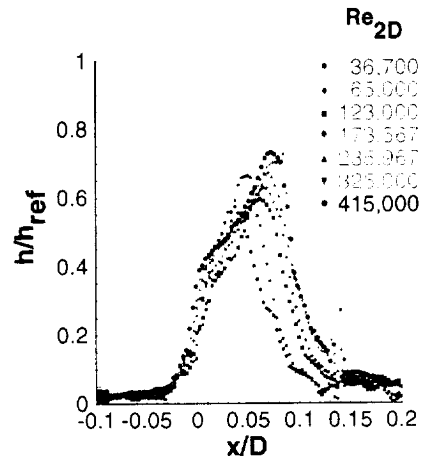

Figure 10. Effect of Reynolds number on normalized impingement zone heating along MSRO afterbody. M_∞=6, air, ρ_2/ρ_∞=5, α= -4 degrees.

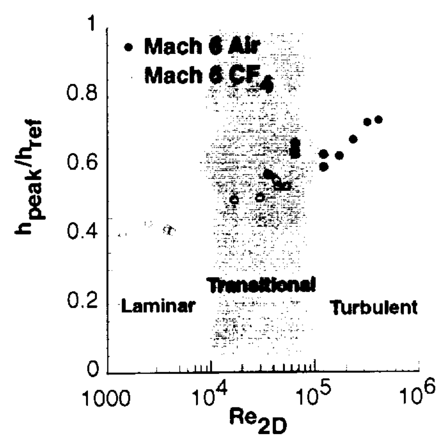

Figure 11. Effect of Reynolds number on normalized impingement heating peak on MSRO afterbody. M_∞=6, air and CF_4, α= -4 degrees.

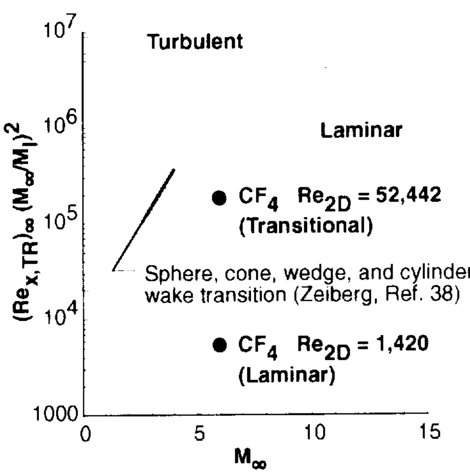

Figure 12. Comparison of present results to a unified wake transition correlation (Ref. 38). M_∞=6, CF_4, α= -4 degrees.

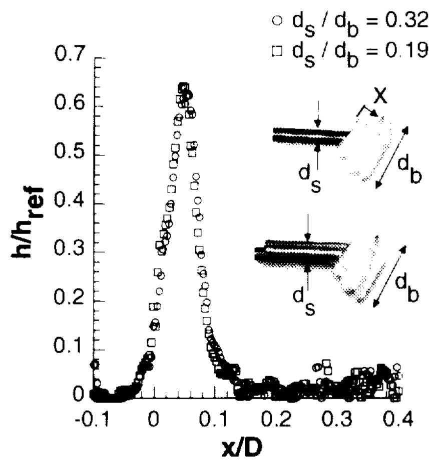

Figure 13. Effect of support sting diameter on normalized MSRO transitional impingement zone heating. M_∞=6, air, Re_{2D}=36,700, α= -4 degrees.

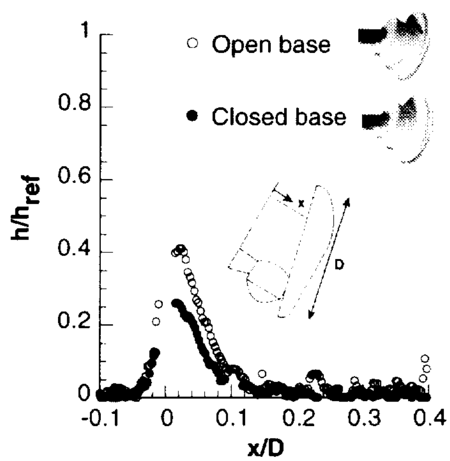

Figure 14. Effect of open and closed MSRO base plane on normalized laminar impingement zone heating. M_∞=6, CF_4, Re_{2D}=3,946, α= -4 degrees.

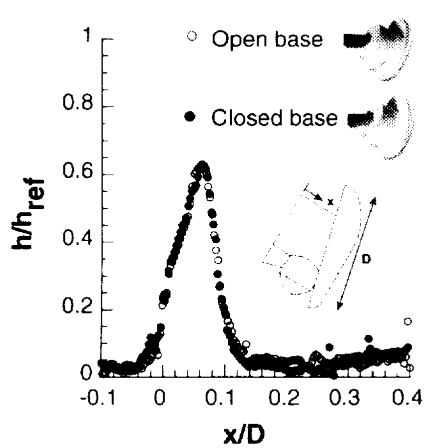

Figure 15. Effect of open and closed MSRO base plane on normalized transitional impingement zone heating. M_∞=6, air, Re_{2D}=52,442, α= -4 degrees.

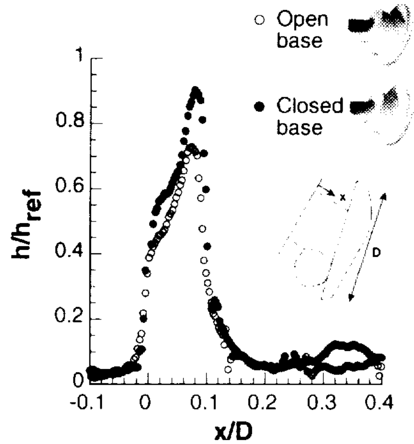

Figure 16. Effect of open and closed MSRO base plane on normalized turbulent impingement zone heating. M_∞=6, air, Re_{2D}=415,000, α= -4 degrees.

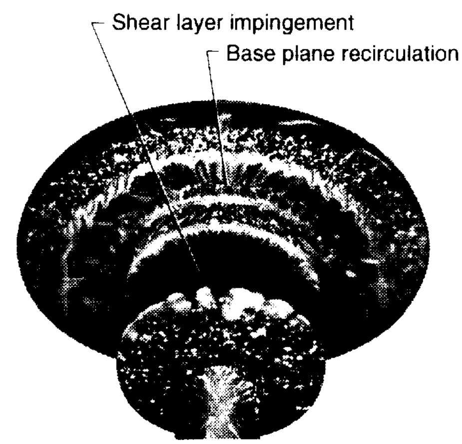

Figure 17. Surface streamlines on closed MSRO base plane in the presence of turbulent shear layer impingement. M_∞=6, air, Re_{2D}=415,000, α= -4 degrees.

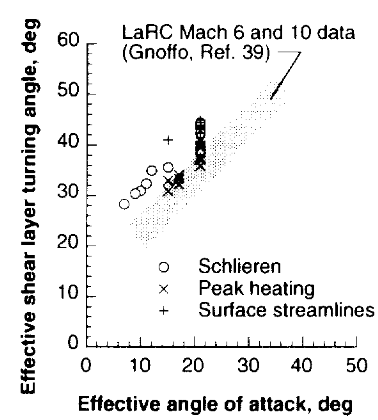

Figure 18. MSRO shear layer turning angle as a function of effective angle of attack. M_∞=6, air, Re_{2D}=36,700 to 415,000.

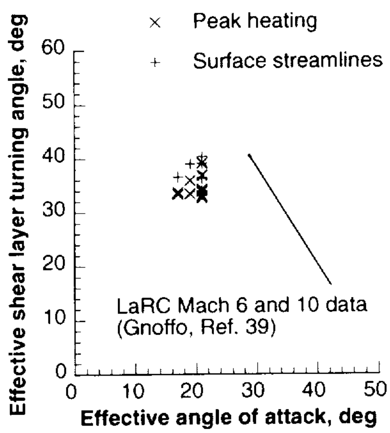

Figure 19. MSRO shear layer turning angle as a function of effective angle of attack. M_∞=6, CF_4, Re_{2D}=1,420 to 52,442.

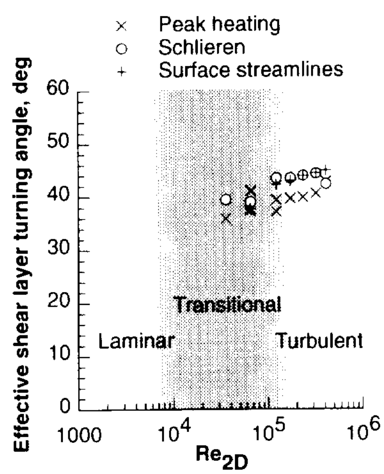

Figure 20. MSRO shear layer turning angle as a function of Reynolds number. M_∞=6, air, α= -4 degrees.

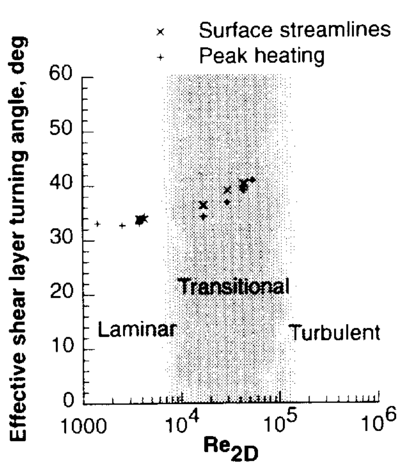

Figure 21. MSRO shear layer turning angle as a function of Reynolds number. M_∞=6, CF_4, α= -4 degrees.

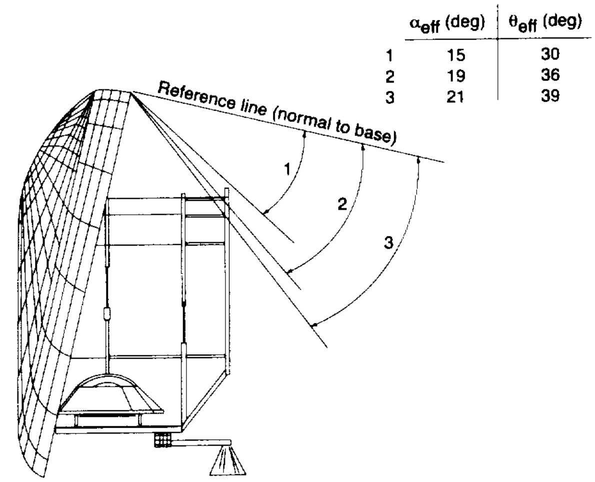

Figure 22. Estimated position of MSRO wake shear layer relative to the afterbody for various effective angles of attack.

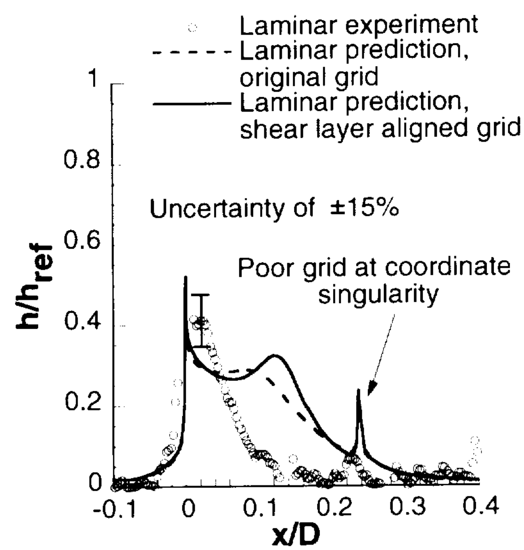

Figure 23. Comparison of measured MSRO laminar impingement zone heating distribution with prediction. M_∞=6, CF_4, Re_{2D}=3,946, α= -4 degrees.